

Interspecies Förster resonances for Rb-Cs Rydberg d -states for enhanced multi-qubit gate fidelitiesP. M. Ireland¹, D. M. Walker¹, and J. D. Pritchard^{1*}*Department of Physics, SUPA, Strathclyde University, Glasgow G4 0NG, United Kingdom*

(Received 4 January 2024; accepted 20 February 2024; published 18 March 2024)

We present an analysis of interspecies interactions between Rydberg d -states of rubidium and cesium. We identify the Förster resonance channels offering the strongest interspecies couplings, demonstrating the viability for performing high-fidelity two- and multi-qubit C_kZ gates up to $k = 4$, including accounting for blockade errors evaluated via numerical diagonalization of the pair potentials. Our results show d -state orbitals offer enhanced suppression of intraspecies couplings compared to s -states, making them well suited for use in large-scale neutral atom quantum processors.

DOI: [10.1103/PhysRevResearch.6.013293](https://doi.org/10.1103/PhysRevResearch.6.013293)

I. INTRODUCTION

Neutral atom arrays provide a versatile platform for performing both programmable quantum simulation and quantum computation [1–4]. Arrays of optical tweezers offer a scalable route to creating deterministically loaded, defect-free qubit registers in up to three dimensions [5–8]. Interactions between qubits can be engineered using highly excited Rydberg states to perform high-fidelity two- and multi-qubit gate operations [9–16] for implementing digital quantum algorithms [17,18] or for encoding solutions to classical optimization problems using coherent quantum annealing [19–21]. Using this architecture for quantum simulation [22,23] has enabled novel topological phases [24] and quantum spin liquids [25] to be observed. Combining these approaches with dynamically reconfigurable tweezers [18] provides a route to observation of fast-scrambling dynamics [26] or efficient implementation of low-density parity check codes for quantum error correction [27], with recent demonstrations of transversal gates between logical qubits making a first step towards fault-tolerant operation [28].

While there has been significant progress to advance two-qubit gate fidelities $\mathcal{F} > 99.5\%$ [29,30] along with recent demonstrations of scalable nondestructive readout [31] and midcircuit measurement [32–34], most experiments have used only a single atomic species. This introduces limitations in localized qubit readout due to cross-talk between atoms and in multi-qubit gate operations where fidelities are limited by parasitic interactions between Rydberg states [13,16,20].

One approach to overcome this limitation is to use dual-species arrays, which naturally provides a separation in readout wavelengths to suppress cross-talk, while allowing

engineering of different inter- and intraspecies couplings. Additionally, this offers a route to universal quantum computation using globally driven pulses [35]. Early work demonstrated two-qubit gates and arrays between different isotopes of rubidium (Rb) [11,36], with recent developments showing continuous loading and measurement feedback onto a cesium (Cs)-Rb array [37,38]. This same approach of using heterogeneous tweezers has enabled assembly of polar molecules [39–43], leading to first demonstrations of hybrid systems [44,45] based on coupling a Rydberg atom to a polar molecule [46].

Previous theoretical work exploring dual-species Rydberg interactions has focused on studying Rydberg interactions in s -state orbitals for Rb-Cs [47] and s and d states for Rb-K atoms [48,49], where suitable Förster resonances have been identified to obtain strong intraspecies couplings with dispersion coefficients calculated in the asymptotic limit. This forms the basis of proposals for quantum nondemolition readout [47], quantum error correction using dual-species surface codes [50], and high-fidelity heteronuclear $C_2\text{NOT}^2$ gates [51], which suppress the unwanted interspecies target-target and control-control interactions.

In this paper we extend the dual-species analysis to study interspecies interactions between Cs and Rb Rydberg atoms in the d -state orbitals, utilizing open source libraries [52,53] for calculating Rydberg-atom interaction potentials via direct diagonalization of the dipole-dipole Hamiltonian to go beyond evaluating the asymptotic dispersion coefficients. We identify suitable Förster resonances for maximizing interspecies coupling strengths, carefully considering the angular dependence to address applications of performing two- and multi-qubit gates in neutral atom arrays for different quantization axis choices as illustrated in Fig. 1. We quantify blockade leakage errors for different Förster-pair states and further evaluate the intrinsic gate errors based on the canonical three-pulse controlled phase gate protocol [54] for C_kZ gates up to $k = 4$, demonstrating enhanced fidelity for multi-qubit operations compared to single-species approaches. We show the advantages of using d -state rather than s -state resonances identified in previous studies due to the inherent reduction

*jonathan.pritchard@strath.ac.uk

Published by the American Physical Society under the terms of the [Creative Commons Attribution 4.0 International](https://creativecommons.org/licenses/by/4.0/) license. Further distribution of this work must maintain attribution to the author(s) and the published article's title, journal citation, and DOI.

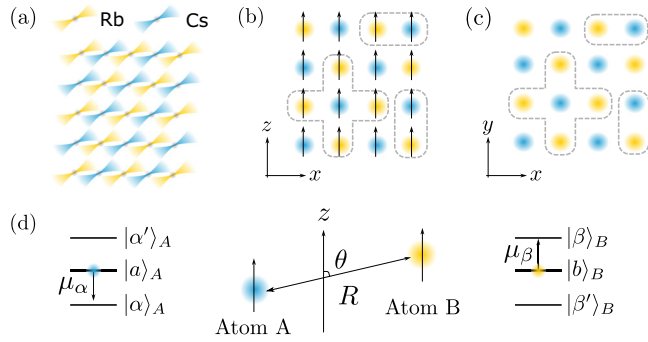


FIG. 1. Dual-species interactions. (a) Schematic of a dual species array of Cs and Rb atoms using state-selective optical tweezers. For performing interspecies CZ or C_4Z gates (indicated by dashed outlines), the orientation of the internuclear axis relative to the quantization axis (\hat{z}) is important, with quantization along the tweezer axis in (b) leading to interactions at a range of angles, while quantization perpendicular to the array plane (c) ensures all interactions occur for $\theta = 90^\circ$. (d) Interaction angle θ relative to the quantization axis, with an example Förster-resonant state occurring when the initial pair state $|a\rangle_A|b\rangle_B$ is dipole coupled to $|\alpha\rangle_A|\beta\rangle_B$ with a small energy defect Δ .

in intraspecies couplings. These results are relevant to teams working in both quantum computation and simulation and provide a guide to appropriate state choice and polarization when designing dual-species experiments.

The paper is organized as follows. In Sec. II we provide a brief introduction to Rydberg atom interactions; then in Sec. III we identify the dominant Förster resonances for the Rb-Cs d -states, studying the angular dependence and comparing to previously identified s -state resonances. In Sec. IV we evaluate the blockade and leakage errors associated with Förster-resonant pairs, considering the performance for achieving both strong blockaded interactions for Rb-Cs pairs and weak intraspecies Rb-Rb and Cs-Cs couplings. From this analysis the Rb $59d_{5/2}$ – Cs $6d_{3/2}$ resonance offers the best performance for extension to C_kZ gates and in Sec. V we provide estimates of gate fidelity, before summarizing our findings in Sec. VI.

II. RYDBERG ATOM INTERACTIONS

To begin we briefly summarize the methods used to calculate Rydberg atom interactions. For a pair of atoms separated by distance R at angle θ with respect to the quantization axis, as illustrated in Fig. 1(b), the dipole-dipole interaction is given by [55]

$$V(R) = \frac{\boldsymbol{\mu}_A \cdot \boldsymbol{\mu}_B - 3(\hat{\mathbf{n}} \cdot \boldsymbol{\mu}_A)(\hat{\mathbf{n}} \cdot \boldsymbol{\mu}_B)}{R^3}, \quad (1)$$

where $\boldsymbol{\mu}_A$ and $\boldsymbol{\mu}_B$ are the electric dipole moments for atom A and atom B, respectively, for coupling target pair states $|a\rangle_A|b\rangle_B$ to pair states $|\alpha\rangle_A|\beta\rangle_B$ and $\hat{\mathbf{n}}$ is the unit vector along the atom separation axis R .

The sign and strength of the resulting interaction is determined by the dipole coupled pair state $|\alpha^A\beta^B\rangle \equiv |\alpha\rangle_A|\beta\rangle_B$, with the smallest energy defect $\Delta = (E_\alpha - E_a) + (E_\beta - E_b)$ with respect to the target pair state $|ab\rangle$. For $|\Delta| \gg V(R)$ the

resulting interaction is in the van der Waals regime of the form with energy shifts scaling as C_6/R^6 , while for $|\Delta| < V(R)$ the system experiences a strong first-order energy shift into branches with energies of $\pm C_3/R^3$. Alternatively, dc electric fields can be used to tune a near-resonant pair to achieve $\Delta = 0$ [56–58].

To estimate the sign and magnitude of the coupling strengths for a given pair state, it is instructive to calculate the $C_{3,k}$ channel coefficient introduced in Ref. [47] defined as

$$C_{3,k} = \frac{e^2}{4\pi\epsilon_0} \frac{\langle \alpha_k || r_A || a \rangle \langle \beta_k || r_B || b \rangle}{\sqrt{(2j_{\alpha_k} + 1)(2j_{\beta_k} + 1)}}, \quad (2)$$

where $|\alpha_k^A\beta_k^B\rangle$ is a Rydberg pair state which is dipole coupled to the target pair state $|\alpha^A\beta^B\rangle$ and $\langle \phi_k || r_X || \psi \rangle$ is the reduced matrix element for transitions between states ψ and ϕ_k in the fine-structure basis for atom X associated with interaction channel k . j_ψ is the total angular momentum quantum number associated to the state ψ .

Asymptotic dispersion coefficients C_6 and C_3 can be calculated by summing over the relevant dipole-coupled pair states [47,59]; however, for the typical atomic separations used in current tweezer array experiments $3 < R < 15 \mu\text{m}$ accurate calculation of the resulting interatomic interactions requires exact diagonalization of the resulting pair-state Hamiltonian including higher-order dipole-quadrupole and quadrupole-quadrupole terms. Below we use the *pair-interaction* library [52] to evaluate Rydberg state couplings, which exploits measured quantum defects and numerical integration of the atomic wave functions based on model potentials to calculate Rydberg state energies and matrix elements, respectively.

To engineer strong interspecies couplings it is necessary to identify Förster resonant pair states that have small energy defects Δ and large coupling strengths $C_{3,k}$ [47]. For two independent species or isotopes, this is achieved by choosing relevant quantum numbers including principal quantum number and orbital angular momentum, resulting in a large degree of tunability and control in choosing Förster resonant pairs. For the intraspecies couplings, however, the energy defects of a given pair are determined entirely by the inherent quantum defects for each species, meaning there is typically only a single value of n which is near resonant and that predominantly the intraspecies interactions are in the weaker van der Waals regime which drops off rapidly with R .

III. RUBIDIUM-CESIUM d -STATE FÖRSTER RESONANCES

We identify suitable Förster-resonant pairs of Rb and Cs in d orbital angular momentum states by calculating the energy defect Δ and channel coefficient $C_{3,k}$ for all dipole-coupled pair states from atoms initially in $d_{3/2}$ or $d_{5/2}$. Due to the large number of possible Förster resonant pair states, we follow the approach of Ref. [47] to consider only resonances with $50 \leq n \leq 90$ that have $|C_{3,k}| > 1 \text{ GHz } \mu\text{m}^3$ and an energy defect $|\Delta| < 0.005$ of the level spacing. Complete tables of resonances are given in the Appendixes, but we focus here on identifying the dominant channels for different combinations of values of the total angular momentum quantum number j .

A. Rb $d_{5/2}$ – Cs $d_{5/2}$

The $n_{\text{Rb}}d_{5/2}n_{\text{Cs}}d_{5/2}$ pair states are dipole coupled through a total of nine possible channels associated with angular quantum numbers of $n'_{\text{Rb}}p_{3/2}n'_{\text{Cs}}p_{3/2}$, $n'_{\text{Rb}}f n'_{\text{Cs}}p_{3/2}$, $n'_{\text{Rb}}p_{3/2}n'_{\text{Cs}}f$, and $n'_{\text{Rb}}f n'_{\text{Cs}}f$, where the f states can be either the $j = 5/2$ or $j = 7/2$ magnetic sublevels. From the resonances listed in Table II there is only a single resonance via the $n'_{\text{Rb}}p_{3/2}n'_{\text{Cs}}p_{3/2}$ channel, while the strongest coupling coefficients $C_{3,k}$ occur for the $(n_{\text{Rb}} + 1)p_{3/2}(n_{\text{Cs}} - 2)f_{7/2}$ channel. Additional dominant channels are $(n_{\text{Rb}} - 2)f(n_{\text{Cs}} - 2)f$ and $(n_{\text{Rb}} - 2)f(n_{\text{Cs}} + 2)p_{3/2}$.

Using these states we now examine the characteristic pair potentials for each of these channels via direct matrix diagonalization, calculating potentials for $\theta = 0^\circ$ and considering atoms in magnetic sublevels $m_j^{\text{Rb}} = m_j^{\text{Cs}} = +5/2$. For the $(n_{\text{Rb}} - 2)f(n_{\text{Cs}} - 2)f$ channel, Fig. 2(a) shows the coupling for Rb $72d_{5/2}$ – Cs $63d_{5/2}$, which is resonant with Rb $70f$ – Cs $61f$ states with $\Delta/2\pi = 19.1\text{MHz}$, with data point intensity colored to reflect the overlap of the target state with the calculated eigenstate $|\phi_i\rangle$ as $|\langle rr|\phi_i\rangle|^2$. While this resonance possesses a strong channel coefficient of $|C_{3,k}| = 7.64\text{GHz}\mu\text{m}^3$, it is evident that rather than a strong resonant interaction at short range ($R < 10\mu\text{m}$), the off-resonant coupling to other pair states suppresses the shift of the upper excitation branch, leading to a weak interaction that is poorly suited to realizing strongly blocked excitation.

In Fig. 2(b) we show the Rb $74d_{5/2}$ – Cs $82d_{5/2}$ state, which is near resonant with Rb $72f$ – Cs $84p_{3/2}$ states. Around $R = 4\text{--}6\mu\text{m}$ we observe the f states split due to coupling with other branches, resulting in a strongly shifted upper excitation branch and mixing in a third eigenstate that is only

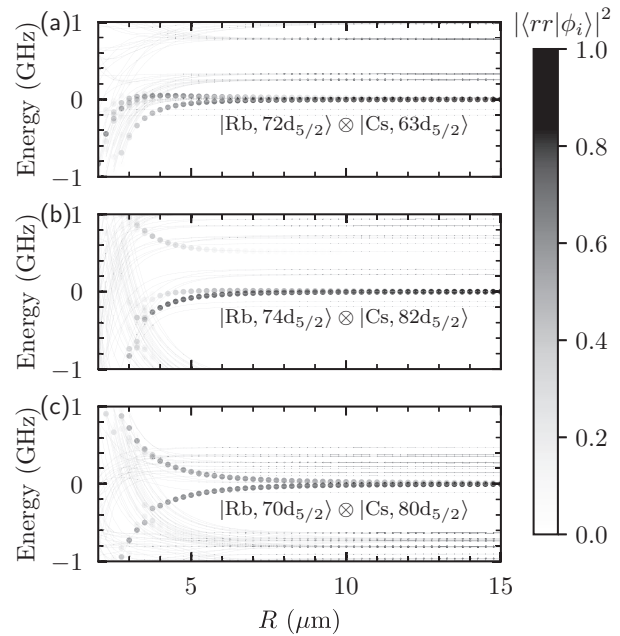


FIG. 2. Example Rb-Cs $n_{\text{Rb}}d_{5/2}n_{\text{Cs}}d_{5/2}$ resonances. (a) Rb $72d_{5/2}$ – Cs $63d_{5/2}$, resonant with Rb $70f$ – Cs $61f$, (b) Rb $74d_{5/2}$ – Cs $82d_{5/2}$, resonant with Rb $72f$ – Cs $84p_{3/2}$, and (c) Rb $70d_{5/2}$ – Cs $80d_{5/2}$, resonant with Rb $71p_{3/2}$ – Cs $78f$. Calculated for $\theta = 0^\circ$ and $m_j^{\text{Rb}} = m_j^{\text{Cs}} = +5/2$.

weakly shifted and preventing use of the $(n_{\text{Rb}} - 2)f(n_{\text{Cs}} + 2)p_{3/2}$ resonances for high-fidelity gates.

In Fig. 2(c) we show the $72d_{5/2}$ – Cs $80d_{5/2}$, which is strongly coupled to the resonant Rb $72f$ – Cs $84p_{3/2}$ states

TABLE I. Summary of the strongest Rb-Cs d -state Förster resonances offering $P_{1r}(t_\pi) \sim 0.999$ for a pair of Rb-Cs atoms separated by $R = 6\mu\text{m}$ calculated at 90° for $(m_j^{\text{Rb}}, m_j^{\text{Cs}}) = (+j^{\text{Rb}}, -j^{\text{Cs}})$ assuming a single-photon Rabi frequency of $\Omega/2\pi = 2\text{MHz}$ compared against the blockade errors expected for multi-qubit gates due to intraspecies coupling for Rb-Rb and Cs-Cs atoms at $8.5\mu\text{m}$. Along with the asymptotic pair energy defect Δ and channel coefficient $C_{3,k}$, we give the effective \tilde{C}_3 and \tilde{C}_6 coefficients obtained by fitting the pair potentials in the region $4 < R < 15\mu\text{m}$. States labeled with an asterisk (*) are suitable for multi-qubit gate with weak intraspecies couplings. Also shown is the only s -state resonance achieving $P_{1r}(t_\pi) > 0.999$.

Rb-Cs Förster resonances		$\Delta/2\pi$	$C_{3,k}$	Rb-Cs at $R = 6\mu\text{m}$		Rb-Rb at $R = 8.5\mu\text{m}$		Cs-Cs at $R = 8.5\mu\text{m}$	
Target pair	Resonant pair	(MHz)	($\text{GHz}\mu\text{m}^3$)	$P_{1r}(t_\pi)$	\tilde{C}_3 ($\text{GHz}\mu\text{m}^3$)	$P_{rr}(t_\pi)$	\tilde{C}_6 ($\text{GHz}\mu\text{m}^6$)	$P_{rr}(t_\pi)$	\tilde{C}_6 ($\text{GHz}\mu\text{m}^6$)
*55 $d_{5/2}$ – 63 $d_{5/2}$	56 $p_{3/2}$ – 61 $f_{5/2}$	12.66	–2.24	0.9969	–11.30	0.9989	21.5	0.9840	–98.8
62 $d_{5/2}$ – 71 $d_{5/2}$	63 $p_{3/2}$ – 69 $f_{5/2}$	–9.53	–3.66	0.9997	15.79	0.9855	64.1	0.7747	–416.8
69 $d_{5/2}$ – 79 $d_{5/2}$	70 $p_{3/2}$ – 77 $f_{7/2}$	–19.14	–21.97	0.9998	26.34	0.7855	192.8	0.0013	–1448.9
70 $d_{5/2}$ – 80 $d_{5/2}$	71 $p_{3/2}$ – 78 $f_{7/2}$	13.69	–23.21	0.9990	–29.03	0.7442	223.9	0.0238	–1812.1
76 $d_{5/2}$ – 87 $d_{5/2}$	77 $p_{3/2}$ – 85 $f_{5/2}$	–19.30	–8.41	0.9997	40.58	0.1156	450.0	0.0388	–4482.5
*52 $d_{5/2}$ – 60 $d_{3/2}$	53 $p_{3/2}$ – 58 $f_{5/2}$	15.19	–6.70	0.9964	–8.37	0.9997	12.2	0.9958	–45.0
*59 $d_{5/2}$ – 68 $d_{3/2}$	60 $p_{3/2}$ – 66 $f_{5/2}$	13.40	–11.23	0.9992	–14.36	0.9951	41.6	0.9410	–206.1
66 $d_{5/2}$ – 76 $d_{3/2}$	67 $p_{3/2}$ – 74 $f_{5/2}$	11.12	–17.74	0.9997	–22.84	0.9176	114.4	0.4467	–692.9
79 $d_{5/2}$ – 91 $d_{3/2}$	80 $p_{3/2}$ – 89 $f_{5/2}$	–12.53	–36.95	0.9999	49.07	0.0070	619.2	0.0052	–3596.5
80 $d_{5/2}$ – 92 $d_{3/2}$	81 $p_{3/2}$ – 90 $f_{5/2}$	7.42	–38.76	0.9999	–51.12	0.0233	705.2	0.0144	–5756.9
*53 $d_{3/2}$ – 60 $d_{5/2}$	54 $p_{1/2}$ – 58 $f_{5/2}$	–4.41	–1.97	0.9968	7.12	0.9989	19.7	0.9938	–57.00
76 $d_{3/2}$ – 87 $d_{5/2}$	77 $p_{3/2}$ – 85 $f_{5/2}$	6.49	2.81	0.9986	–52.91	0.0129	723.9	0.0186	–5038.3
65 $d_{3/2}$ – 74 $d_{5/2}$	66 $p_{1/2}$ – 72 $f_{5/2}$	–13.07	–17.02	0.9974	16.67	0.7416	234.6	0.8297	–375.1
73 $d_{3/2}$ – 83 $d_{3/2}$	74 $p_{1/2}$ – 81 $f_{5/2}$	–0.70	–27.26	0.9995	28.54	0.1360	452.0	0.1082	–2156.1
80 $d_{3/2}$ – 91 $d_{3/2}$	81 $p_{1/2}$ – 89 $f_{5/2}$	–13.66	–39.62	0.9998	48.51	0.0440	1263.6	0.0234	–3178.2
81 $d_{3/2}$ – 92 $d_{3/2}$	82 $p_{1/2}$ – 90 $f_{5/2}$	4.39	–41.55	0.9997	–47.30	0.0590	1411.2	0.0153	–3836.9
72 $s_{1/2}$ – 70 $s_{1/2}$	71 $p_{3/2}$ – 70 $p_{1/2}$	–7.90	8.51	0.9992	9.82	0.0040	–1106.6	0.4005	–605.3

TABLE II. Rb-Cs Förster resonances from Rb $d_{5/2}$ – Cs $d_{5/2}$ states with $|\Delta|/2\pi < 20$ MHz and $|C_{3,k}| > 1$ GHz μm^3 . $P_{1r}(t_\pi)$ and $P_{rr}(t_\pi)$ along with fitted \tilde{C}_3 and \tilde{C}_6 coefficients are calculated for $\theta = 90^\circ$ and $(m_j^{\text{Rb}}, m_j^{\text{Cs}}) = (5/2, -5/2)$ assuming $\Omega/2\pi = 2$ MHz.

Rb-Cs Förster resonances		$\Delta/2\pi$	$C_{3,k}$	Rb-Cs at $R = 6 \mu\text{m}$		Rb-Rb at $R = 8.5 \mu\text{m}$		Cs-Cs at $R = 8.5 \mu\text{m}$	
Target pair	Resonant pair	(MHz)	(GHz μm^3)	$P_{1r}(t_\pi)$	\tilde{C}_3 (GHz μm^3)	$P_{rr}(t_\pi)$	\tilde{C}_6 (GHz μm^6)	$P_{rr}(t_\pi)$	\tilde{C}_6 (GHz μm^6)
$55d_{5/2} - 53d_{5/2}$	$57p_{3/2} - 50f_{7/2}$	18.71	-2.73	0.9860	-3.13	0.9989	21.4	0.9999	-7.4
$55d_{5/2} - 63d_{5/2}$	$56p_{3/2} - 61f_{5/2}$	12.66	-2.24	0.9969	-11.30	0.9989	21.5	0.9840	-98.8
$55d_{5/2} - 61d_{5/2}$	$53f_{7/2} - 63p_{3/2}$	-12.19	-1.78	0.9747	2.08	0.9989	21.4	0.9923	-62.1
$62d_{5/2} - 71d_{5/2}$	$63p_{3/2} - 69f_{5/2}$	-9.53	-3.66	0.9997	15.79	0.9855	64.1	0.7747	-416.8
$69d_{5/2} - 79d_{5/2}$	$70p_{3/2} - 77f_{7/2}$	-19.14	-21.97	0.9998	26.34	0.7855	192.8	0.0013	-1448.9
$69d_{5/2} - 66d_{5/2}$	$71p_{3/2} - 63f_{5/2}$	-4.29	-1.79	0.9933	7.49	0.7855	192.8	0.9538	-164.5
$77d_{5/2} - 88d_{5/2}$	$78p_{3/2} - 86f_{7/2}$	1.91	-34.24	0.9998	-47.42	0.2966	393.5	0.0282	-4303.1
$74d_{5/2} - 82d_{5/2}$	$72f_{7/2} - 84p_{3/2}$	5.63	-6.15	0.9967	-16.85	0.3269	367.5	0.1115	-2258.4
$70d_{5/2} - 80d_{5/2}$	$71p_{3/2} - 78f_{7/2}$	13.69	-23.21	0.9990	-29.03	0.7442	223.9	0.0238	-1812.1
$76d_{5/2} - 87d_{5/2}$	$77p_{3/2} - 85f_{5/2}$	-19.30	-8.41	0.9997	40.58	0.1156	450.0	0.0388	-4482.5
$84d_{5/2} - 80d_{5/2}$	$86p_{3/2} - 77f_{7/2}$	11.74	-15.58	0.9996	-24.33	0.0514	1318.7	0.0148	-1692.0
$80d_{5/2} - 70d_{5/2}$	$78f_{7/2} - 68f_{5/2}$	-18.70	3.05	0.9932	2.38	0.0229	698.0	0.8301	-356.6
$83d_{5/2} - 79d_{5/2}$	$85p_{3/2} - 76f_{7/2}$	-10.78	-14.80	0.9975	12.46	0.0957	1108.5	0.0013	-1448.9

with $|C_{3,k}| = 23$ GHz μm^3 . This reveals the expected symmetric splitting and $1/R^3$ scaling, making the $(n_{\text{Rb}} + 1)p_{3/2}(n_{\text{Cs}} - 2)f_{7/2}$ resonances ideal for engineering strong interspecies couplings at $\theta = 0^\circ$. These results highlight the importance not only of evaluating the pair defects and channel couplings, but also examining the real pair curves over the desired separation ranges.

B. Rb $d_{3/2}$ – Cs $d_{3/2}$

For the Rb $d_{3/2}$ – Cs $d_{3/2}$ states there are again nine possible channels associated with orbital angular momentum quantum numbers of $n'_{\text{Rb}}pn'_{\text{Cs}}p$, $n'_{\text{Rb}}pn'_{\text{Cs}}f_{5/2}$, $n'_{\text{Rb}}f_{5/2}n'_{\text{Cs}}p$, and $n'_{\text{Rb}}f_{5/2}n'_{\text{Cs}}f_{5/2}$, where p can be either $j = 1/2$ or $3/2$. Table III shows the filtered resonances, with the strongest $|C_{3,k}|$ channel coupling via the $(n_{\text{Rb}} + 1)p_{1/2}(n_{\text{Cs}} - 2)f_{5/2}$ resonances.

In Fig. 3 example resonances for the different channels are plotted, with similar behavior observed as for the $d_{5/2} - d_{5/2}$ resonances where the channels with pair states resonant with Rb $f_{5/2}$ states [shown in (a) and (b)] provide unsuitable resonances at short range. The strongest resonance is for Rb $73d_{3/2}$ – Cs $83d_{3/2}$, which is coupled to Rb $74p_{1/2}$ – Cs $81f_{5/2}$ with $\Delta/2\pi = -0.84$ MHz and $C_{3,k} = -27.3$ GHz μm^3 plotted in Fig. 3(c) showing a strong Förster resonant coupling at short range, with similar behavior observed for resonances for pairs involving the Rb $p_{3/2}$ state but with a weaker coupling due to the larger defects. At short range ($R < 5 \mu\text{m}$), comparing the result here to the approximately equivalent resonance shown in Fig. 2(c) at comparable quantum numbers, the $d_{3/2} - d_{3/2}$ resonance mixes with more pair states than the $d_{5/2} - d_{5/2}$ case, leading to the two characteristic branches splitting with the target pair state now appearing across a larger number of pair eigenstates.

C. Rb $d_{3/2}$ – Cs $d_{5/2}$ and Rb $d_{5/2}$ – Cs $d_{3/2}$

Förster resonances for the Rb $d_{3/2}$ – Cs $d_{5/2}$ and Rb $d_{5/2}$ – Cs $d_{3/2}$ states are presented in Tables V and IV, respectively. These mixed j pairs follow a similar trend to those above, with

the strongest resonances observed for $(n_{\text{Rb}} + 1)p_{j_{\text{Rb}}-1}(n_{\text{Cs}} - 2)f_{j_{\text{Cs}}+1}$ couplings and resonances with Rb p and Cs f states producing the desired $1/R^3$ resonant splitting at $\theta = 0^\circ$. In comparison to the Rb $d_{3/2}$ – Cs $d_{5/2}$ states, Rb $d_{5/2}$ – Cs $d_{3/2}$ pairs typically have larger Δ values; however, there are more states with strong $C_{3,k}$ at lower values of n_{Rb} .

As will be shown below in Sec. V, the resonances via Rb $d_{3/2}$ states are also less favorable for scaling to multi-qubit interactions due to the presence of a near Förster resonance for Rb $58d_{3/2}$ –Rb $58d_{3/2}$, leading to anomalously large intraspecies C_6 coefficients for nearby $n_{\text{Rb}}d_{3/2}$ states.

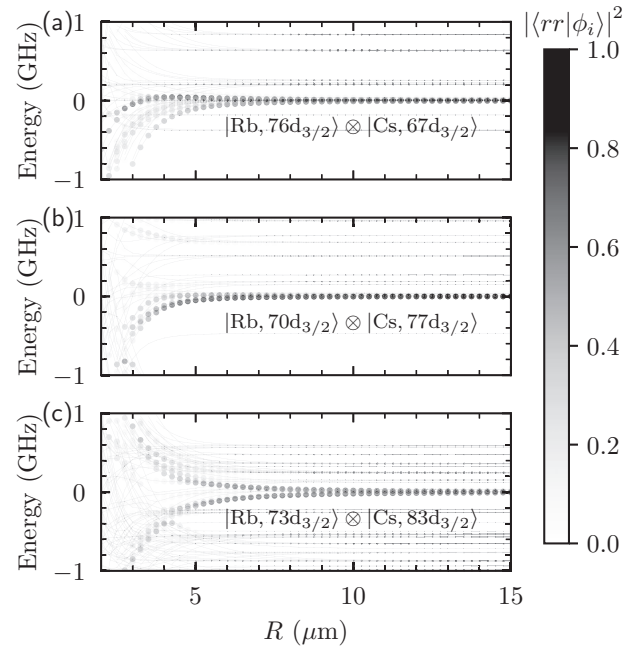


FIG. 3. Example Rb $d_{3/2}$ – Cs $d_{3/2}$ Förster resonances. (a) Rb $76d_{3/2}$ – Cs $67d_{3/2}$, resonant with Rb $74f_{5/2}$ – Cs $65f_{5/2}$, (b) Rb $70d_{3/2}$ – Cs $77d_{3/2}$, resonant with Rb $68f_{5/2}$ – Cs $79p_{1/2}$, and (c) Rb $73d_{3/2}$ – Cs $83d_{3/2}$, resonant with Rb $74p_{1/2}$ – Cs $81f_{5/2}$. Calculated for $\theta = 0^\circ$ and $m_j^{\text{Rb}} = m_j^{\text{Cs}} = +3/2$.

TABLE III. Rb-Cs Förster resonances from Rb $d_{3/2}$ – Cs $d_{3/2}$ states with $|\Delta|/2\pi < 20$ MHz and $|C_{3,k}| > 1$ GHz μm^3 . $P_{1r}(t_\pi)$ and $P_{rr}(t_\pi)$ along with fitted \tilde{C}_3 and \tilde{C}_6 coefficients are calculated for $\theta = 90^\circ$ and $(m_j^{\text{Rb}}, m_j^{\text{Cs}}) = (3/2, -3/2)$ assuming $\Omega/2\pi = 2$ MHz.

Rb-Cs Förster resonances		$\Delta/2\pi$	$C_{3,k}$	Rb-Cs at $R = 6 \mu\text{m}$		Rb-Rb at $R = 8.5 \mu\text{m}$		Cs-Cs at $R = 8.5 \mu\text{m}$	
Target pair	Resonant pair	(MHz)	(GHz μm^3)	$P_{1r}(t_\pi)$	\tilde{C}_3 (GHz μm^3)	$P_{rr}(t_\pi)$	\tilde{C}_6 (GHz μm^6)	$P_{rr}(t_\pi)$	\tilde{C}_6 (GHz μm^6)
51 $d_{3/2}$ - 59 $d_{3/2}$	52 $p_{3/2}$ - 57 $f_{5/2}$	-18.12	2.08	0.9912	0.83	0.9995	13.8	0.9995	-15.8
50 $d_{3/2}$ - 57 $d_{3/2}$	51 $p_{1/2}$ - 55 $f_{5/2}$	16.13	-5.82	0.9958	-6.33	0.9997	11.4	0.9998	-10.9
51 $d_{3/2}$ - 62 $d_{3/2}$	50 $f_{5/2}$ - 59 $f_{5/2}$	-15.98	4.52	0.9814	3.15	0.9995	13.8	0.9995	-13.2
65 $d_{3/2}$ - 75 $d_{3/2}$	66 $p_{3/2}$ - 73 $f_{5/2}$	8.32	5.58	0.9955	-36.55	0.7416	234.6	0.7704	-440.2
69 $d_{3/2}$ - 66 $d_{3/2}$	71 $p_{1/2}$ - 63 $f_{5/2}$	-6.16	-7.35	0.9979	6.81	0.4719	224.4	0.9706	-141.0
64 $d_{3/2}$ - 61 $d_{3/2}$	66 $p_{3/2}$ - 58 $f_{5/2}$	3.96	1.64	0.8913	-0.35	0.7767	211.9	0.9939	-63.6
65 $d_{3/2}$ - 74 $d_{3/2}$	66 $p_{1/2}$ - 72 $f_{5/2}$	-13.07	-17.02	0.9974	16.67	0.7416	234.6	0.8297	-375.1
76 $d_{3/2}$ - 67 $d_{3/2}$	74 $f_{5/2}$ - 65 $f_{5/2}$	2.04	8.99	0.9868	-12.99	0.0129	723.9	0.9587	-163.3
77 $d_{3/2}$ - 73 $d_{3/2}$	79 $p_{3/2}$ - 70 $f_{5/2}$	-6.12	3.50	0.9789	3.82	0.0692	820.6	0.8729	-308.5
71 $d_{3/2}$ - 79 $d_{3/2}$	69 $f_{5/2}$ - 81 $p_{3/2}$	9.09	1.63	0.9944	-11.82	0.2858	329.2	0.3238	-545.4
70 $d_{3/2}$ - 77 $d_{3/2}$	68 $f_{5/2}$ - 79 $p_{1/2}$	7.97	-5.30	0.9961	-10.84	0.3789	287.4	0.6138	-629.1
72 $d_{3/2}$ - 83 $d_{3/2}$	73 $p_{3/2}$ - 81 $f_{5/2}$	10.33	8.46	0.9985	-42.76	0.2049	390.5	0.1082	-2156.1
79 $d_{3/2}$ - 91 $d_{3/2}$	80 $p_{3/2}$ - 89 $f_{5/2}$	10.38	12.33	0.9998	-51.08	0.1280	1112.0	0.0234	-3178.2
78 $d_{3/2}$ - 90 $d_{3/2}$	79 $p_{3/2}$ - 88 $f_{5/2}$	-10.66	11.75	0.9998	21.39	0.1607	957.1	0.0262	-2568.1
73 $d_{3/2}$ - 83 $d_{3/2}$	74 $p_{1/2}$ - 81 $f_{5/2}$	-0.70	-27.26	0.9995	28.54	0.1360	452.0	0.1082	-2156.1
81 $d_{3/2}$ - 92 $d_{3/2}$	82 $p_{1/2}$ - 90 $f_{5/2}$	4.39	-41.55	0.9997	-47.30	0.0590	1411.2	0.0153	-3836.9
84 $d_{3/2}$ - 74 $d_{3/2}$	82 $f_{5/2}$ - 72 $f_{5/2}$	-8.89	13.56	0.9906	3.10	0.0368	1937.6	0.6502	-484.5
84 $d_{3/2}$ - 80 $d_{3/2}$	86 $p_{1/2}$ - 77 $f_{5/2}$	11.47	-16.47	0.9953	-24.02	0.0368	1937.6	0.7637	-388.1
80 $d_{3/2}$ - 89 $d_{3/2}$	78 $f_{5/2}$ - 91 $p_{3/2}$	4.98	2.68	0.9966	-21.96	0.0440	1263.6	0.0135	-2640.7
80 $d_{3/2}$ - 88 $d_{3/2}$	78 $f_{5/2}$ - 90 $p_{1/2}$	-3.06	-9.23	0.9357	9.12	0.0440	1263.6	0.0007	-2226.4
80 $d_{3/2}$ - 91 $d_{3/2}$	81 $p_{1/2}$ - 89 $f_{5/2}$	-13.66	-39.62	0.9998	48.51	0.0440	1263.6	0.0234	-3178.2
83 $d_{3/2}$ - 79 $d_{3/2}$	85 $p_{1/2}$ - 76 $f_{5/2}$	-10.65	-15.65	0.9983	10.75	0.0603	1610.2	0.0904	-1035.9

D. Angular dependence

In the analysis above we consider atoms at $\theta = 0^\circ$, which results in the total magnetic quantum number $M = m_j^A + m_j^B$ being preserved by the dipole-dipole interaction with $\Delta M = 0$ selection rules. For experiments in 2D tweezer arrays, this condition is only met for the case of atoms oriented with the internuclear axis along the quantization axis. For

performing multi-qubit gate operations, or exploiting long-range couplings for quantum simulation, placing a quantization axis parallel to one of the axis coordinates results in atoms interacting across a range of angles from $\theta = 0^\circ$ to 90° as shown in Fig. 1(b). Alternatively, the quantization axis can be aligned normal to the array plane, meaning all atoms interact at 90° as shown in Fig. 1(c), providing an isotropic coupling of

 TABLE IV. Rb-Cs Förster resonances from Rb $d_{5/2}$ – Cs $d_{3/2}$ states with $|\Delta|/2\pi \lesssim 20$ MHz and $|C_{3,k}| > 1$ GHz μm^3 . $P_{1r}(t_\pi)$ and $P_{rr}(t_\pi)$ along with fitted \tilde{C}_3 and \tilde{C}_6 coefficients are calculated for $\theta = 90^\circ$ and $(m_j^{\text{Rb}}, m_j^{\text{Cs}}) = (5/2, -3/2)$ assuming $\Omega/2\pi = 2$ MHz.

Rb-Cs Förster resonances		$\Delta/2\pi$	$C_{3,k}$	Rb-Cs at $R = 6 \mu\text{m}$		Rb-Rb at $R = 8.5 \mu\text{m}$		Cs-Cs at $R = 8.5 \mu\text{m}$	
Target pair	Resonant pair	(MHz)	(GHz μm^3)	$P_{1r}(t_\pi)$	\tilde{C}_3 (GHz μm^3)	$P_{rr}(t_\pi)$	\tilde{C}_6 (GHz μm^6)	$P_{rr}(t_\pi)$	\tilde{C}_6 (GHz μm^6)
59 $d_{5/2}$ - 68 $d_{3/2}$	60 $p_{3/2}$ - 66 $f_{5/2}$	13.40	-11.23	0.9992	-14.36	0.9951	41.6	0.9410	-206.1
50 $d_{5/2}$ - 37 $d_{3/2}$	49 $f_{7/2}$ - 38 $p_{1/2}$	-5.91	-2.93	0.9864	3.87	0.9999	8.2	1.0000	-0.2
52 $d_{5/2}$ - 60 $d_{3/2}$	53 $p_{3/2}$ - 58 $f_{5/2}$	15.19	-6.70	0.9964	-8.37	0.9997	12.2	0.9958	-45.0
66 $d_{5/2}$ - 76 $d_{3/2}$	67 $p_{3/2}$ - 74 $f_{5/2}$	11.12	-17.74	0.9997	-22.84	0.9176	114.4	0.4467	-692.9
68 $d_{5/2}$ - 60 $d_{3/2}$	66 $f_{5/2}$ - 58 $f_{5/2}$	-8.50	1.52	0.9272	3.71	0.8373	170.4	0.9993	-18.9
60 $d_{5/2}$ - 66 $d_{3/2}$	58 $f_{7/2}$ - 68 $p_{1/2}$	-14.00	-2.87	0.9906	2.65	0.9929	48.3	0.9698	-144.1
67 $d_{5/2}$ - 49 $d_{3/2}$	66 $f_{7/2}$ - 50 $p_{1/2}$	-5.80	-9.64	0.9932	11.22	0.8889	142.5	1.0000	-2.7
78 $d_{5/2}$ - 74 $d_{3/2}$	80 $p_{3/2}$ - 71 $f_{5/2}$	2.73	-11.14	0.9977	-16.52	0.0056	557.1	0.8297	-375.1
79 $d_{5/2}$ - 91 $d_{3/2}$	80 $p_{3/2}$ - 89 $f_{5/2}$	-12.53	-36.95	0.9999	49.07	0.0070	619.2	0.0052	-3596.5
73 $d_{5/2}$ - 84 $d_{3/2}$	74 $p_{3/2}$ - 82 $f_{5/2}$	9.09	-26.72	0.9949	-36.07	0.4852	314.6	0.1085	-2230.7
77 $d_{5/2}$ - 56 $d_{3/2}$	76 $f_{7/2}$ - 57 $p_{1/2}$	-20.99	-16.90	0.9912	17.86	0.2966	393.5	0.9996	-14.4
81 $d_{5/2}$ - 90 $d_{3/2}$	79 $f_{7/2}$ - 92 $p_{3/2}$	16.57	2.90	0.9953	-19.25	0.0649	765.4	0.0024	-3282.6
83 $d_{5/2}$ - 73 $d_{3/2}$	81 $f_{5/2}$ - 71 $f_{5/2}$	15.70	3.43	0.9939	-12.68	0.0957	1108.5	0.8729	-308.5
81 $d_{5/2}$ - 89 $d_{3/2}$	79 $f_{5/2}$ - 91 $p_{1/2}$	5.56	-2.58	0.9802	-23.45	0.0858	839.1	0.0261	-2866.1
84 $d_{5/2}$ - 61 $d_{3/2}$	86 $f_{7/2}$ - 61 $p_{3/2}$	-6.70	-0.00	0.9991	26.62	0.0774	1227.1	0.9939	-63.6
80 $d_{5/2}$ - 92 $d_{3/2}$	81 $p_{3/2}$ - 90 $f_{5/2}$	7.42	-38.76	0.9999	-51.12	0.0233	705.2	0.0144	-5756.9

TABLE V. Rb-Cs Förster resonances from Rb $d_{3/2}$ – Cs $d_{5/2}$ states with $|\Delta|/2\pi \lesssim 20$ MHz and $|C_{3,k}| > 1$ GHz μm^3 . $P_{1r}(t_\pi)$ and $P_{rr}(t_\pi)$ along with fitted \tilde{C}_3 and \tilde{C}_6 coefficients are calculated for $\theta = 90^\circ$ and $(m_j^{\text{Rb}}, m_j^{\text{Cs}}) = (3/2, -5/2)$ assuming $\Omega/2\pi = 2$ MHz.

Rb-Cs Förster resonances		$\Delta/2\pi$	$C_{3,k}$	Rb-Cs at $R = 6 \mu\text{m}$		Rb-Rb at $R = 8.5 \mu\text{m}$		Cs-Cs at $R = 8.5 \mu\text{m}$	
Target pair	Resonant pair	(MHz)	(GHz μm^3)	$P_{1r}(t_\pi)$	\tilde{C}_3 (GHz μm^3)	$P_{rr}(t_\pi)$	\tilde{C}_6 (GHz μm^6)	$P_{rr}(t_\pi)$	\tilde{C}_6 (GHz μm^6)
$59d_{3/2} - 57d_{5/2}$	$61p_{1/2} - 54f_{5/2}$	2.93	-1.03	0.9823	-5.56	0.6608	187.8	0.9981	-32.2
$53d_{3/2} - 60d_{5/2}$	$54p_{1/2} - 58f_{5/2}$	-4.41	-1.97	0.9968	7.12	0.9989	19.7	0.9938	-57.0
$64d_{3/2} - 71d_{5/2}$	$62f_{5/2} - 73p_{3/2}$	4.08	-3.26	0.9909	-7.31	0.7767	211.9	0.7383	-435.9
$78d_{3/2} - 88d_{5/2}$	$79p_{1/2} - 86f_{5/2}$	6.51	-9.49	0.9915	-39.56	0.1607	957.1	0.0085	-5492.7
$76d_{3/2} - 87d_{5/2}$	$77p_{3/2} - 85f_{5/2}$	6.49	2.81	0.9986	-52.91	0.0129	723.9	0.0186	-5038.3
$80d_{3/2} - 70d_{5/2}$	$78f_{5/2} - 68f_{5/2}$	3.69	2.95	0.9920	-11.62	0.0440	1263.6	0.8048	-377.9
$83d_{3/2} - 79d_{5/2}$	$85p_{3/2} - 76f_{7/2}$	8.93	4.92	0.9918	-32.33	0.0522	1813.4	0.0000	-1466.9
$90d_{3/2} - 86d_{5/2}$	$92p_{1/2} - 83f_{5/2}$	2.55	-5.81	0.9961	-40.04	0.0066	3762.9	0.0201	-4212.1

an atom to its neighbors, where at this angle $V(R)$ couples pair states with $\Delta M = 0, \pm 2$. In this section we explore the angular dependence of the d -state Förster resonances, considering the impact on choice of magnetic sublevel. All calculations below are performed using a magnetic field of 6 G [31] to define the quantization axis.

Figure 4 shows angular potentials for the Förster resonance between Rb $55d_{5/2}$ – Cs $63d_{5/2}$ for different combinations

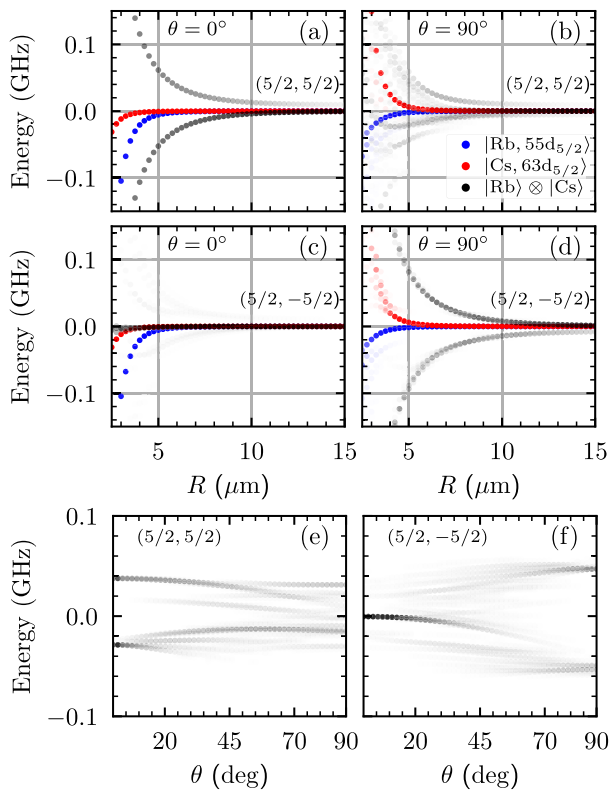


FIG. 4. Angular dependence of the Rb $55d_{5/2}$ – Cs $63d_{5/2}$ Förster resonance for different $(m_j^{\text{Rb}}, m_j^{\text{Cs}})$. (a) $\theta = 0^\circ$, $(5/2, 3/2)$, (b) $\theta = 90^\circ$, $(5/2, 5/2)$, (c) $\theta = 0^\circ$, $(5/2, -5/2)$, and (d) $\theta = 90^\circ$, $(5/2, -5/2)$. Interspecies pair potentials are plotted black with opacity proportional to state overlap. Also shown are intraspecies interaction curves for Rb-Rb in $55d_{5/2}$ (red) and Cs-Cs in $63d_{5/2}$ (blue). (e),(f) The variation of energy eigenstates with θ for $(5/2, \pm 5/2)$ calculated at $R = 6 \mu\text{m}$ revealing the Förster resonance can only be used at 0° and 90° .

of $(m_j^{\text{Rb}}, m_j^{\text{Cs}}) = (5/2, \pm 5/2)$ and for angles $\theta = 0^\circ$ and 90° . Considering first the $(5/2, 5/2)$ combination, Fig. 4(a) shows at 0° we obtain a strong Förster resonance splitting; however, at 90° the additional coupling terms driving $\Delta M = \pm 2$ cause the target Rydberg states to be mixed with a large number of other pair eigenstates, several of which have weak or vanishing interaction shifts. Conversely, for the $(5/2, -5/2)$ combination with $M = 0$ we see a strong suppression of the interaction at 0° in Fig. 4(c) leading to a flat potential curve for $R > 5 \mu\text{m}$ due to the presence of a Förster zero in the interaction channel [60], while for 90° we recover the desired Förster splitting as shown in Fig. 4(d). Comparing the results in (a) and (d) shows that the $\theta = 90^\circ$ offers improved symmetry between upper and lower excitation branches of the pair potentials with respect to the unshifted pair state, extending the useful blockade range which is limited by the smallest shift of either branch. This shows that operation at 90° with a $(5/2, -5/2)$ combination is preferable not only for achieving isotropic couplings across the array, but also for improved long-range interactions.

Alongside the Rb-Cs pair potentials, the figures also show intraspecies interaction curves for Rb $55d_{5/2} - 55d_{5/2}$ in blue and Cs $63d_{5/2} - 63d_{5/2}$ in red. For both Figs. 4(a) and 4(d) with strong interspecies Förster resonance, we see the intraspecies interaction curves remain flat until $R \lesssim 5 \mu\text{m}$ before showing a van der Waals like C_6/R^6 shift. Despite having a lower quantum number of $n_{\text{Rb}} = 55$, the Rb-Rb C_6 coefficient is comparable to that of the $n_{\text{Cs}} = 63$ due to the Rb quantum defects yielding smaller pair defects for the intraspecies d -states than that of Cs. This also shows the advantage of using dual-species interactions, with the Rb-Cs coupling offering a strong blocked interaction at $R = 6 \mu\text{m}$, where the intraspecies coupling is negligible.

For intermediate angles, Figs. 4(e) and 4(f) show the pair-state eigenenergies as a function of θ calculated for a separation of $R = 6 \mu\text{m}$. Unlike the characteristic $C_3 \propto [1 - 3 \cos^2(\theta)]$ dependence obtained for single-species couplings between atoms in identical states [61], the angular profiles show that operating more than around 5° away from the optimal values of $\theta = 0^\circ$ and $\pi/2$ the pair potentials show a complex energy landscape with a large number of additional eigenstates appearing that have weak or vanishing energy shifts, preventing realization of strong blocked interactions at these intermediate angles.

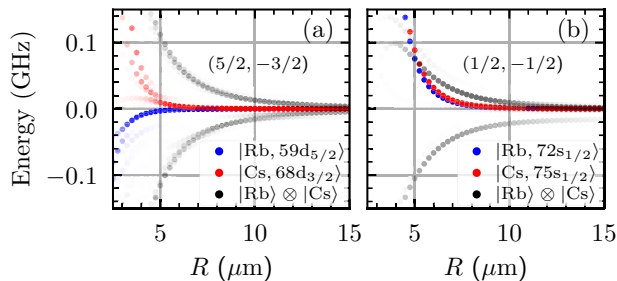


FIG. 5. Comparison of d and s state Förster resonances with $\theta = 90^\circ$ with magnetic sublevels denoted $(m_j^{\text{Rb}}, m_j^{\text{Cs}})$. (a) Rb $59d_{5/2}$ – Cs $68d_{3/2}$ Förster resonance for $(5/2, -3/2)$ and (b) Rb $72s_{1/2}$ – Cs $75s_{1/2}$ Förster resonance for $(1/2, -1/2)$. Interspecies pair potentials are plotted black with opacity proportional to state overlap. Intraspecies interaction curves are shown for Rb (red) and Cs (blue).

For the other interaction channels, a similar behavior is observed with stable resonances observed for $(m_j^{\text{Rb}}, m_j^{\text{Cs}}) = (+j^{\text{Rb}}, +j^{\text{Cs}})$ at $\theta = 0^\circ$ and $(+j^{\text{Rb}}, -j^{\text{Cs}})$ at 90° . An example resonance for the Rb $59d_{5/2}$ – Cs $68d_{3/2}$ resonance at $\theta = 90^\circ$ and $(5/2, -3/2)$ is shown in Fig. 5(a), which provides one of the best states for achieving low blockade and leakage errors as detailed later.

E. Comparison to s -state Förster resonances

To illustrate the advantage of the d -state resonances over s -states, Fig. 5(b) shows an example Förster resonance for the Rb $72s_{1/2}$ – Cs $70s_{1/2}$ state previously identified in Ref. [47] for $\theta = 90^\circ$ and $(m_j^{\text{Rb}}, m_j^{\text{Cs}}) = (1/2, -1/2)$. This reveals a strong interspecies resonance with comparable magnitude to that of Rb $59d_{5/2}$ – Cs $68d_{3/2}$ shown in Fig. 5(a), but with the downside being that the intraspecies Rb-Rb and Cs-Cs interactions have a similar magnitude, negating the advantage of being able to exploit strong Rb-Cs interaction while suppressing the intraspecies couplings.

A further benefit is that, when performing two-photon excitation to the Rydberg states, the dipole-matrix elements to the intermediate state scale as $n^{-3/2}$. As well as obtaining comparable interspecies interactions at lower principal quantum numbers, the d -states have a prefactor in this scaling approximately twice as strong as the s -states yielding enhanced Rabi frequencies at the same laser power.

IV. BLOCKADE LEAKAGE ERRORS

In order to exploit Rydberg atom interactions for performing high-fidelity controlled gate operations, we use the blockade regime where the interaction strength V greatly exceeds the excitation linewidth determined by the Rabi frequency Ω describing the rate of coupling from the computational ground state to the target Rydberg state, preventing more than a single Rydberg excitation from being created.

For the Förster resonances identified above, the exact pair potentials include coupling not just to a single level, but to many pair eigenstates $|\phi_i\rangle$ each with energy ϵ_i , and it is necessary to consider not only the blockade effect arising from the strongly shifted eigenstates but also blockade leakage due to coupling to weakly shifted eigenstates. To determine the

blockade leakage error for a given target pair state $|r_i^A, r_i^B\rangle$, we calculate the probability of exciting this double Rydberg state following a resonant π pulse applied to atom A for atoms initialized at time $t = 0$ in the state $|\Psi(0)\rangle = |1^A, r_i^B\rangle$, where $|1^A\rangle$ is the computational state of atom A, taking into account coupling to all possible eigenstates $|\phi_i\rangle$ found through diagonalizing the pair state interactions.

The Hamiltonian for the coupled system is given by

$$\hat{H} = \hbar \sum_{i=1} \left(\left[\frac{\eta_i \Omega}{2} |\phi_i\rangle \langle 0^A, r_i^B| + \text{H.c.} \right] - \epsilon_i |\phi_i\rangle \langle \phi_i| \right), \quad (3)$$

where Ω is the Rabi frequency for coupling $|1^A\rangle \rightarrow |r_i^A\rangle$ and $\eta_i = \langle r_i^A, r_i^B | \phi_i \rangle$ denotes the relative overlap of the target pair state with the energy eigenstate, and the sum is taken for all eigenstates with $|\eta_i| > 10^{-3}$. The resulting wave function at time t is given by $|\Psi(t)\rangle = e^{-i\hat{H}t/\hbar} |\Psi(0)\rangle$, from which the probability of a double Rydberg excitation is given by

$$P_{rr}(t) = \sum_{i=1} |\langle \phi_i | \Psi(t) \rangle|^2 \quad (4)$$

and the probability of finding the atom in the initial ground state is $P_{1r}(t) = |\langle 1^A, r_i^B | \Psi(t) \rangle|^2$.

For each of the possible Förster-resonant pairs, we evaluate the blockade leakage error calculated for an Rb-Cs pair at a spacing of $R = 6 \mu\text{m}$ for $\theta = 90^\circ$ and using $(+m_j^{\text{Rb}}, -m_j^{\text{Cs}})$ following application of a resonant π pulse for assuming a value of $\Omega/2\pi = 2\text{MHz}$. Results are presented in Table I, which is filtered to select states with $P_{1r}(t_\pi) > 0.999$ consistent with strong blockade and leakage errors below 10^{-3} . For the Rb $d_{3/2}$ – Cs $d_{5/2}$ interactions no pair states reach this limit, with two example resonances included for completeness, while for the other interaction channels several candidate pair states are identified with leakage errors as low as 10^{-4} for Rb $79d_{5/2}$ – Cs $91d_{3/2}$ and Rb $80d_{5/2}$ – Cs $92d_{3/2}$.

Since one of the motivations for using dual species interactions is not only to obtain strong Rb-Cs couplings, but also to provide a route to realizing multiqubit gates suppressing target-target and control-control couplings, we additionally consider the impact of intraspecies interactions. We assume atoms are arranged on a square lattice as shown in Fig. 1 and calculate the probability of creating doubly excited Rb-Rb and Cs-Cs pair states at a minimum distance of $\sqrt{2}R = 8.5 \mu\text{m}$. For these states we evaluate both the probability of creating a double excitation after a π pulse and of returning back to the initial state following a 2π pulse, which in the ideal case of zero intraspecies interactions would return unity in both cases. We also tabulate the effective \tilde{C}_3 and \tilde{C}_6 coefficients obtained by fitting the dominant interaction curves in the region $4 < R < 15 \mu\text{m}$ for the Rb-Cs, Rb-Rb, and Cs-Cs interaction curves to enable extrapolation of the interaction strength within these distances typically used for tweezer experiments.

From Table I it can be seen that, while many suitable Rb-Cs Förster resonances can be found, those offering the highest suppression of blockade leakage typically correspond to states with higher principal quantum number ($n \gtrsim 65$), where the residual intraspecies interactions at $8.5 \mu\text{m}$ are sufficiently strong that there is a significant blockade effect visible for the Rb-Rb and Cs-Cs curves, making these poorly suited to extension to multi-qubit gates. While in practice these errors

can be suppressed to some extent by using increased single-photon Rabi frequencies, this comes at the cost of increased leakage errors for the Rb-Cs interactions. This also highlights the limitations of using $n_{\text{Rb}}d_{3/2}$ states above, as from the table it can be seen that for $n_{\text{Rb}} \geq 58$ these have a much stronger blockade error for Rb-Rb than the comparable $n_{\text{Rb}}d_{5/2}$ states. For completeness we note only a single s -state resonance achieves $P_{1r}(t_\pi) > 0.999$ for which the resulting Rb-Rb and Cs-Cs interactions are too strongly blocked for use for multi-qubit gates in agreement with the pair potential shown above in Fig. 5(b).

Imposing the requirement to not only obtain low leakage errors for Rb-Cs but also reduced errors for Rb-Rb and Cs-Cs operations, we identify a number of possible states denoted by an asterisk in the table that balance the different error channels. From these candidates $55d_{5/2}63d_{5/2}$, $52d_{5/2}60d_{3/2}$, and $53d_{3/2}60d_{5/2}$ offer comparable performance of $P > 0.99$ for all metrics and $59d_{5/2}68d_{3/2}$ achieves the lowest intraspecies error with $P_{rr}(t_\pi) = 0.995$ for Rb-Rb while achieving $P_{1r}(t_\pi) > 0.999$ for Rb-Cs. In the next section we use this state to estimate realistic multi-qubit gate performance.

V. DUAL-SPECIES MULTI-QUBIT GATE OPERATIONS

In the analysis above the only error considered in performing gate operations has been that of blockade errors due to errors associated with leakage of population into doubly occupied states for the Rb-Cs interactions and the suppression of doubly occupied states for the Rb-Rb and Cs-Cs case due to residual intraspecies couplings. To accurately estimate gate fidelity, it is necessary to also include errors associated with spontaneous emission from the Rydberg state as well as scattering from the intermediate excited state during the two-photon excitation of atoms to the Rydberg state.

To efficiently simulate these errors, we adopt the effective model introduced in Ref. [16] to model each atom using three computational levels with an effective single-atom Hamiltonian describing atom-light interactions of the form

$$\hat{H}_{\text{eff}} = \frac{\hbar}{2} \left[-iP_e^l \Gamma_e |1\rangle \langle 1| + \Omega_R (|r\rangle \langle 1| + |1\rangle \langle r|) - (\delta + i\Gamma_r + P_e^r \Gamma_e) |r\rangle \langle r| \right], \quad (5)$$

where Ω_R is the effective two-photon Rabi frequency, δ is the two-photon detuning, $\Gamma_{e,r}$ are the excited and Rydberg state linewidths, and P_e^l and P_e^r are excited state probabilities determined from performing adiabatic elimination of the intermediate excited states. For gates performed using the Rb $59d_{5/2}$ – Cs $68d_{3/2}$ Förster resonance, we first determine suitable parameters for the two-photon Rabi frequency to ensure atoms obtain a π -phase shift when excited through 2π by tuning the ratio between the two-photon Rabi frequencies [10]. For both species, we assume a single-photon detuning of 10 GHz from the excited state transition and determine parameters giving $\Omega_R/2\pi = 5\text{MHz}$. For Rb, excitations are modeled via the $6p_{3/2}$ intermediate state with $\Gamma_e/2\pi = 1.4\text{MHz}$ and for Cs via $7p_{1/2}$ with $\Gamma_e/2\pi = 1.0\text{MHz}$. Full details of the excitation parameters are given in Appendix B.

Using the effective Hamiltonian, we model the canonical phase-gate protocol based on a π pulse on the control qubit, followed by a 2π pulse on the target and a third π pulse on the control qubit for an initial symmetric superposition of all possible input states. We note that, while this is not an optimal pulse sequence, it provides a simple approach to extending to C^kZ gates yielding the correct output states up to single qubit rotations [13]. For these diagonal controlled phase gates, this also enables efficient estimation of the resulting gate fidelity by calculating $\mathcal{F} = |\langle \Psi_I | \Psi \rangle|^2$, where $|\Psi\rangle$ is the final wave function and $|\Psi_I\rangle$ is the output of an ideal gate.

We first consider a two-qubit CZ gate for Rb-Cs atoms separated by $R = 6\text{ }\mu\text{m}$, which experience an interaction shift of $V_{\text{Rb-Cs}}/2\pi = 65.6\text{MHz}$. Using Rb as the control qubit gives $\mathcal{F}_{CZ} = 0.9953$, while for Cs as the control qubit $\mathcal{F}_{CZ} = 0.9955$, which is competitive against recent experimental demonstrations [29,30]. Scaling to multi-qubit gates, we recall that this pair state was chosen due to the suppressed Rb-Rb interactions and proceed to use a single Cs target atom and increase the number of neighboring Rb control atoms.

For the CCZ gate, placing atoms on a line with the Rb control atoms on either side of a central Cs target, the Rb-Rb interaction at $16\text{ }\mu\text{m}$ corresponds to $V_{\text{Rb-Rb}}/2\pi = 0.11\text{MHz}$, resulting in $\mathcal{F}_{CCZ} = 0.994$, while moving the second Rb control atom to the site below the Cs (at a reduced Rb-Rb distance of $8.5\text{ }\mu\text{m}$) increases the control-control coupling to $V_{\text{Rb-Rb}}/2\pi = 0.14\text{MHz}$ and results in $\mathcal{F}_{CCZ} = 0.983$. Extending to a C^3Z gate with three Rb atoms in an equilateral triangle configuration with the Cs atom at the center gives $\mathcal{F}_{C^3Z} = 0.988$ and for the square geometry shown in Fig. 1(c) we find a C^4Z gate gives $\mathcal{F}_{C^4Z} = 0.913$.

While even with the engineered interspecies interactions we still observe a reduction in fidelity due to residual intraspecies coupling, decomposition of the CCZ gate requires 6 CZ operations [62], which would require $\mathcal{F}_{CZ} > 0.999$ and 0.997 , respectively, for the line and square configurations, demonstrating the benefit of using dual-species couplings for native multi-qubit gate implementations. Additionally, further optimization of gate pulses taking account of additional technical noise sources could yield higher gate performance, but lies beyond the scope of this current work.

VI. CONCLUSION

In this paper we have presented a detailed analysis of the d -state Förster resonances for engineering strong Rb-Cs interactions to enable high-fidelity gate operations between heterogeneous atom pairs. We have identified dominant interaction channels yielding strong $C_{3,k}$ coefficients and small pair defects and demonstrated the importance of performing diagonalization of the pair-state potentials to identify suitable resonances for achieving strong short-range interactions.

From studying the angular dependence of the pair potentials we have shown that for the d -states the Förster resonances are only robust at $\theta = 0^\circ$ or 90° dependent upon the choice of magnetic sublevel, with $(+m_j^{\text{Rb}}, -m_j^{\text{Cs}})$ providing the best performance at $\theta = 90^\circ$, but with additional benefits compared to the s -state resonances through much greater suppression of the intraspecies interactions and

providing stronger resonant interactions at lower principal quantum number.

By calculating blockade leakage and excitation errors using the full pair-state eigenvalues, we have identified states offering the best performance for realizing robust blockade for controlled gate operations and demonstrated the ability to use these strong interspecies couplings to realize high-fidelity C^kZ gates due to suppression of the residual intraspecies couplings between control qubits compared to single-species gate implementations, providing a route to native multi-qubit gates with performance exceeding that expected for the equivalent two-qubit gate decompositions using current best-known protocols [16,29].

These results highlight the potential advantages of developing scalable neutral atom processors based on dual atomic species and will guide future demonstrations of gate operations on these emerging Rb-Cs platforms [37,46] by providing improved choice over the best Förster-resonant pair states to target.

The data presented in the paper are available here [63].

ACKNOWLEDGMENTS

This work was funded by the Royal Academy of Engineering Senior Research Fellowship with M Squared Lasers and the Engineering and Physical Sciences Research Council (Grant No. EP/X025055/1).

APPENDIX A: TABLES OF RB-CS d -STATE FÖRSTER RESONANCES

In Tables II to V we present $n_{\text{Rb}}d_j - n_{\text{Cs}}d_j$ Förster resonant pair states with $|\Delta|/2\pi \lesssim 20\text{MHz}$ and $|C_{3,k}| > 1 \text{ GHz } \mu\text{m}^3$ for the different combinations of $j = 3/2, 5/2$. For each state we additionally show $P_{1r}(t_\pi)$ for Rb-Cs at $R = 6 \mu\text{m}$ to quantify blockade leakage errors and $P_{rr}(t_\pi)$ for Rb-Rb and Cs-Cs interactions at $R = 8.5 \mu\text{m}$ representative of expected errors for dual-species multi-qubit gates on a square grid. Finally, we include the dispersion coefficients \tilde{C}_3 and \tilde{C}_6 for inter- and intraspecies couplings respectively obtained by fitting the pair eigenstate with the largest target state probability in the region $5 \leq R \leq 15 \mu\text{m}$. For comparison Table VI includes the pa-

rameters obtained for s -state Förster-resonant pairs previously identified in Ref. [47], which typically have higher leakage errors than the d -states and much stronger blockade error for intraspecies couplings with similar magnitude and range as the Rb-Cs coupling.

APPENDIX B: TWO-PHOTON EXCITATION PARAMETERS

In this paper we consider interactions between d -orbital Rydberg states of Cs and Rb which are created using a two-photon excitation process via an intermediate excited state. To include the effects of excitation and spontaneous decay from the intermediate states, we use the simplified effective Hamiltonian introduced in Eq. (5), which is obtained by performing adiabatic elimination of excited state hyperfine levels f_e requiring calculation of the following terms [16]:

$$\Omega_R = \sum_{f_e} \frac{\Omega_1^{f_e} \Omega_{f_e}^r}{2\Delta_{f_e}}, \quad (\text{B1})$$

$$\delta_{\text{AC}} = \sum_{f_e} \frac{|\Omega_1^{f_e}|^2 - |\Omega_{f_e}^r|^2}{4\Delta_{f_e}}, \quad (\text{B2})$$

$$P_e^l = \sum_{f_e} \frac{|\Omega_1^{f_e}|^2}{4\Delta_{f_e}^2}, \quad (\text{B3})$$

$$P_e^r = \sum_{f_e} \frac{|\Omega_{f_e}^r|^2}{4\Delta_{f_e}^2}, \quad (\text{B4})$$

where Ω_R is the effective two-photon Rabi frequency, Δ_{f_e} is the single-photon detuning with respect to the intermediate hyperfine level, and $P_e^{l,r}$ is the residual excited state population due to coupling between the ground and Rydberg state transitions, respectively.

Using this effective model to represent the transition from $|1\rangle$ and $|r\rangle$ to appear as a spin-1/2 system enforces the desired result that after a 2π rotation the wave function acquires a π -phase shift. However, for a real two-photon excitation with multiple intermediate excited states, the exact phase $\phi_{2\pi}$ accumulated after a 2π pulse can take any value between $0-2\pi$ dependent upon the relative power of the lasers and

TABLE VI. Rb-Cs Förster resonances from Rb $s_{1/2} - \text{Cs } s_{1/2}$ states previously identified [47]. $P_{1r}(t_\pi)$ and $P_{rr}(t_\pi)$ along with fitted \tilde{C}_3 and \tilde{C}_6 coefficients are calculated for $\theta = 90^\circ$ and $(m_j^{\text{Rb}}, m_j^{\text{Cs}}) = (1/2, -1/2)$ assuming $\Omega/2\pi = 2\text{MHz}$.

Rb-Cs Förster resonances		$\Delta/2\pi$ (MHz)	$C_{3,k}$ (GHz μm^3)	Rb-Cs at $R = 6 \mu\text{m}$		Rb-Rb at $R = 8.5 \mu\text{m}$		Cs-Cs at $R = 8.5 \mu\text{m}$	
Target pair	Resonant pair			$P_{1r}(t_\pi)$	\tilde{C}_3 (GHz μm^3)	$P_{rr}(t_\pi)$	\tilde{C}_6 (GHz μm^6)	$P_{rr}(t_\pi)$	\tilde{C}_6 (GHz μm^6)
$48s_{1/2} - 51s_{1/2}$	$48p_{3/2} - 50p_{1/2}$	-5.53	1.69	0.6281	3.00	0.9998	-9.5	0.9996	-14.5
$59s_{1/2} - 57s_{1/2}$	$58p_{1/2} - 57p_{1/2}$	-16.45	3.54	0.3752	1.35	0.9767	-114.2	0.9943	-56.6
$69s_{1/2} - 68s_{1/2}$	$68p_{1/2} - 68p_{3/2}$	-9.89	6.92	0.9959	12.69	0.3230	-701.2	0.6503	-430.2
$68s_{1/2} - 67s_{1/2}$	$67p_{1/2} - 67p_{3/2}$	2.63	6.50	0.9727	-9.12	0.4660	-594.3	0.7432	-367.5
$61s_{1/2} - 65s_{1/2}$	$61p_{1/2} - 64p_{1/2}$	2.77	4.80	0.9735	-2.62	0.9487	-168.9	0.8689	-263.5
$72s_{1/2} - 75s_{1/2}$	$72p_{1/2} - 74p_{3/2}$	2.70	9.65	0.9835	-12.40	0.0040	-1106.6	0.0359	-1187.3
$77s_{1/2} - 81s_{1/2}$	$77p_{3/2} - 80p_{1/2}$	-2.10	12.28	0.9969	16.42	0.0100	-2103.4	0.0344	-2151.8
$72s_{1/2} - 70s_{1/2}$	$71p_{3/2} - 70p_{1/2}$	-7.90	8.51	0.9992	9.82	0.0040	-1106.6	0.4005	-605.3
$71s_{1/2} - 69s_{1/2}$	$70p_{3/2} - 69p_{1/2}$	9.45	8.01	0.9987	-10.66	0.0643	-955.7	0.5348	-518.5

intermediate state detuning [10]. To ensure accurate parameters are chosen for estimating the gate fidelity with the effective model, for each of the transitions in Cs and Rb we first generate an exact single atom model including all excited states without adiabatic elimination and adjust the power ratios in the two lasers to tune the system to give an error in the phase shift of $|\phi_{2\pi} - \pi| < 10^{-5}$.

For both transitions we calculate single-photon Rabi frequencies $\Omega_1^{f_e}$ and $\Omega_1^{r_e}$ assuming a center of mass detuning from the intermediate state of 10 GHz, targeting a two-photon Rabi frequency of $\Omega_R/2\pi = 5\text{MHz}$ typical of recent experimental demonstrations and quote powers for a beam waist of 10 μm to allow easy scaling to other beam parameters.

Excitation in Rb from $|1\rangle = |2, 0\rangle$ to $|r\rangle = |59d_{5/2}, m_j = 5/2\rangle$ with $\Gamma_r/2\pi = 0.76\text{kHz}$ is modeled using transitions via the $6p_{3/2}$ intermediate state with $\Gamma_e/2\pi = 1.4\text{MHz}$ using a pair of σ^+ -polarized photons. Choosing powers of 20 mW and 150 mW for the lower and upper transitions results in a π -phase shift with $P_e^{1,r} = (5.0, 1.7) \times 10^{-4}$, respectively. Excitation in Cs from $|1\rangle = |4, 0\rangle$ to $|r\rangle = |68d_{3/2}, m_j = -3/2\rangle$ with $\Gamma_r/2\pi = 0.86\text{kHz}$ is modeled using transitions via the $7p_{1/2}$ intermediate state with $\Gamma_e/2\pi = 1.0\text{MHz}$ using a pair of σ^- -polarized photons. Choosing powers of 5.2 mW and 240 mW for the lower and upper transitions results in a π -phase shift with $P_e^{1,r} = (5.0, 1.2) \times 10^{-4}$, respectively.

-
- [1] M. Saffman, T. G. Walker, and K. Mølmer, Quantum information with Rydberg atoms, *Rev. Mod. Phys.* **82**, 2313 (2010).
- [2] C. S. Adams, J. D. Pritchard, and J. P. Shaffer, Rydberg atom quantum technologies, *J. Phys. B* **53**, 012002 (2019).
- [3] A. Browaeys and T. Lahaye, Many-body physics with individually controlled Rydberg atoms, *Nat. Phys.* **16**, 132 (2020).
- [4] M. Morgado and S. Whitlock, Quantum simulation and computing with Rydberg-interacting qubits, *AVS Quantum Sci.* **3**, 023501 (2021).
- [5] M. Endres, H. Bernien, A. Keesling, H. Levine, E. R. Anschuetz, A. Krajenbrink, C. Senko, V. Vuletić, M. Greiner, and M. D. Lukin, Atom-by-atom assembly of defect-free one-dimensional cold atom arrays, *Science* **354**, 1024 (2016).
- [6] D. Barredo, S. de Léséleuc, V. Lienhard, T. Lahaye, and A. Browaeys, An atom-by-atom assembler of defect-free arbitrary two-dimensional atomic arrays, *Science* **354**, 1021 (2016).
- [7] D. Barredo, V. Lienhard, S. de Léséleuc, T. Lahaye, and A. Browaeys, Synthetic three-dimensional atomic structures assembled atom by atom, *Nature (London)* **561**, 79 (2018).
- [8] A. Kumar, T.-Y. Wu, F. Giraldo, and D. S. Weiss, Sorting ultracold atoms in a three-dimensional optical lattice in a realization of Maxwell's demon, *Nature (London)* **561**, 83 (2018).
- [9] L. Isenhower, E. Urban, X. L. Zhang, A. T. Gill, T. Henage, T. A. Johnson, T. G. Walker, and M. Saffman, Demonstration of a neutral atom controlled-not quantum gate, *Phys. Rev. Lett.* **104**, 010503 (2010).
- [10] K. M. Maller, M. T. Lichtman, T. Xia, Y. Sun, M. J. Piotrowicz, A. W. Carr, L. Isenhower, and M. Saffman, Rydberg-blockade controlled-not gate and entanglement in a two-dimensional array of neutral-atom qubits, *Phys. Rev. A* **92**, 022336 (2015).
- [11] Y. Zeng, P. Xu, X. He, Y. Liu, M. Liu, J. Wang, D. J. Papoular, G. V. Shlyapnikov, and M. Zhan, Entangling two individual atoms of different isotopes via Rydberg blockade, *Phys. Rev. Lett.* **119**, 160502 (2017).
- [12] T. M. Graham, M. Kwon, B. Grinkemeyer, Z. Marra, X. Jiang, M. T. Lichtman, Y. Sun, M. Ebert, and M. Saffman, Rydberg mediated entanglement in a two-dimensional neutral atom qubit array, *Phys. Rev. Lett.* **123**, 230501 (2019).
- [13] H. Levine, A. Keesling, G. Semeghini, A. Omran, T. T. Wang, S. Ebadi, H. Bernien, M. Greiner, V. Vuletić, H. Pichler, and M. D. Lukin, Parallel implementation of high-fidelity multi-qubit gates with neutral atoms, *Phys. Rev. Lett.* **123**, 170503 (2019).
- [14] Z. Fu, P. Xu, Y. Sun, Y. Y. Liu, X. D. He, X. Li, M. Liu, R. B. Li, J. Wang, L. Liu, and M. S. Zhan, High fidelity entanglement of neutral atoms via a Rydberg-mediated single-modulated-pulse controlled-PHASE gate, *Phys. Rev. A* **105**, 042430 (2022).
- [15] K. McDonnell, L. F. Keary, and J. D. Pritchard, Demonstration of a quantum gate using electromagnetically induced transparency, *Phys. Rev. Lett.* **129**, 200501 (2022).
- [16] G. Pelegrí, A. J. Daley, and J. D. Pritchard, High-fidelity multi-qubit Rydberg gates via two-photon adiabatic rapid passage, *Quantum Sci. Technol.* **7**, 045020 (2022).
- [17] T. M. Graham, Y. Song, J. Scott, C. Poole, L. Phuttitarn, K. Jooya, P. Eichler, X. Jiang, A. Marra, B. Grinkemeyer, M. Kwon, M. Ebert, J. Cherek, M. T. Lichtman, M. Gillette, J. Gilbert, D. Bowman, T. Ballance, C. Campbell, E. D. Dahl *et al.*, Demonstration of multi-qubit entanglement and algorithms on a programmable neutral atom quantum computer, *Nature (London)* **604**, 457 (2022).
- [18] D. Bluvstein, H. Levine, G. Semeghini, T. T. Wang, S. Ebadi, M. Kalinowski, A. Keesling, N. Maskara, H. Pichler, M. Greiner, V. Vuletić, and M. D. Lukin, A quantum processor based on coherent transport of entangled atom arrays, *Nature (London)* **604**, 451 (2022).
- [19] H. Pichler, S.-T. Wang, L. Zhou, S. Choi, and M. D. Lukin, Quantum optimization for maximum independent set using Rydberg atom arrays, [arXiv:1808.10816](https://arxiv.org/abs/1808.10816) [quant-ph].
- [20] S. Ebadi, A. Keesling, M. Cain, T. T. Wang, H. Levine, D. Bluvstein, G. Semeghini, A. Omran, J.-G. Liu, R. Samajdar, X.-Z. Luo, B. Nash, X. Gao, B. Barak, E. Farhi, S. Sachdev, N. Gemelke, L. Zhou, S. Choi, H. Pichler *et al.*, Quantum optimization of maximum independent set using Rydberg atom arrays, *Science* **376**, 1209 (2022).
- [21] M.-T. Nguyen, J.-G. Liu, J. Wurtz, M. D. Lukin, S.-T. Wang, and H. Pichler, Quantum optimization with arbitrary connectivity using Rydberg atom arrays, *PRX Quantum* **4**, 010316 (2023).
- [22] S. Ebadi, T. T. Wang, H. Levine, A. Keesling, G. Semeghini, A. Omran, D. Bluvstein, R. Samajdar, H. Pichler, W. W. Ho, S. Choi, S. Sachdev, M. Greiner, V. Vuletić, and M. D. Lukin, Quantum phases of matter on a 256-atom programmable quantum simulator, *Nature (London)* **595**, 227 (2021).
- [23] P. Scholl, M. Schuler, H. J. Williams, A. A. Eberharter, D. Barredo, K.-N. Schymik, V. Lienhard, L.-P. Henry, T. C. Lang, T. Lahaye, A. M. Läuchli, and A. Browaeys, Quantum

- simulation of 2D antiferromagnets with hundreds of Rydberg atoms, *Nature (London)* **595**, 233 (2021).
- [24] S. de Léséleuc, V. Lienhard, P. Scholl, D. Barredo, S. Weber, N. Lang, H. Buchler, T. Lahaye, and A. Browaeys, Experimental realization of a symmetry protected topological phase of interacting bosons with Rydberg atoms, *Science* **365**, 775 (2019).
- [25] G. Semeghini, H. Levine, A. Keesling, S. Ebadi, T. T. Wang, D. Bluvstein, R. Verresen, H. Pichler, M. Kalinowski, R. Samajdar, A. Omran, S. Sachdev, A. Vishwanath, M. Greiner, V. Vuletic, and M. D. Lukin, Probing topological spin liquids on a programmable quantum simulator, *Science* **374**, 1242 (2021).
- [26] T. Hashizume, G. S. Bentsen, S. Weber, and A. J. Daley, Deterministic fast scrambling with neutral atom arrays, *Phys. Rev. Lett.* **126**, 200603 (2021).
- [27] Q. Xu, J. P. B. Ataiades, C. A. Pattison, N. Raveendran, D. Bluvstein, J. Wurtz, B. Vasic, M. D. Lukin, L. Jiang, and H. Zhou, Constant-overhead fault-tolerant quantum computation with reconfigurable atom arrays, [arXiv:2308.08648](https://arxiv.org/abs/2308.08648).
- [28] D. Bluvstein, S. J. Evered, A. A. Geim, S. H. Li, H. Zhou, T. Manovitz, S. Ebadi, M. Cain, M. Kalinowski, D. Hangleiter, J. P. Bonilla Ataiades, N. Maskara, I. Cong, X. Gao, P. Sales Rodriguez, T. Karolyshyn, G. Semeghini, M. J. Gullans, M. Greiner, V. Vuletić *et al.*, Logical quantum processor based on reconfigurable atom arrays, *Nature (London)* **626**, 58 (2024).
- [29] S. J. Evered, D. Bluvstein, M. Kalinowski, S. Ebadi, T. Manovitz, H. Zhou, S. H. Li, A. A. Geim, T. T. Wang, N. Maskara, H. Levine, G. Semeghini, M. Greiner, V. Vuletić, and M. D. Lukin, High-fidelity parallel entangling gates on a neutral-atom quantum computer, *Nature (London)* **622**, 268 (2023).
- [30] S. Ma, G. Liu, P. Peng, B. Zhang, S. Jandura, J. Claes, A. P. Burgers, G. Pupillo, S. Puri, and J. D. Thompson, High-fidelity gates with mid-circuit erasure conversion in a metastable neutral atom qubit, *Nature (London)* **622**, 279 (2023).
- [31] B. Nikolov, E. Diamond-Hitchcock, J. Bass, N. L. R. Spong, and J. D. Pritchard, Randomized benchmarking using nondestructive readout in a two-dimensional atom array, *Phys. Rev. Lett.* **131**, 030602 (2023).
- [32] E. Deist, Y.-H. Lu, J. Ho, M. K. Pasha, J. Zeiher, Z. Yan, and D. M. Stamper-Kurn, Mid-circuit cavity measurement in a neutral atom array, *Phys. Rev. Lett.* **129**, 203602 (2022).
- [33] T. M. Graham, L. Phuttitarn, R. Chinnarasu, Y. Song, C. Poole, K. Jooya, J. Scott, A. Scott, P. Eichler, and M. Saffman, Mid-circuit measurements on a single-species neutral alkali atom quantum processor, *Phys. Rev. X* **13**, 041051 (2023).
- [34] J. W. Lis, A. Senoo, W. F. McGrew, F. Rönchen, A. Jenkins, and A. M. Kaufman, Midcircuit operations using the omg architecture in neutral atom arrays, *Phys. Rev. X* **13**, 041035 (2023).
- [35] F. Cesa and H. Pichler, Universal quantum computation in globally driven Rydberg atom arrays, *Phys. Rev. Lett.* **131**, 170601 (2023).
- [36] C. Sheng, J. Hou, X. He, K. Wang, R. Guo, J. Zhuang, B. Mamat, P. Xu, M. Liu, J. Wang, and M. Zhan, Defect-free arbitrary-geometry assembly of mixed-species atom arrays, *Phys. Rev. Lett.* **128**, 083202 (2022).
- [37] K. Singh, S. Anand, A. Pocklington, J. T. Kemp, and H. Bernien, Dual-element, two-dimensional atom array with continuous-mode operation, *Phys. Rev. X* **12**, 011040 (2022).
- [38] K. Singh, C. E. Bradley, S. Anand, V. Ramesh, R. White, and H. Bernien, Mid-circuit correction of correlated phase errors using an array of spectator qubits, *Science* **380**, 1265 (2023).
- [39] L. R. Liu, J. D. Hood, Y. Yu, J. T. Zhang, N. R. Hutzler, T. Rosenband, and K.-K. Ni, Building one molecule from a reservoir of two atoms, *Science* **360**, 900 (2018).
- [40] L. R. Liu, J. D. Hood, Y. Yu, J. T. Zhang, K. Wang, Y.-W. Lin, T. Rosenband, and K.-K. Ni, Molecular assembly of ground-state cooled single atoms, *Phys. Rev. X* **9**, 021039 (2019).
- [41] W. B. Cairncross, J. T. Zhang, L. R. B. Picard, Y. Yu, K. Wang, and K.-K. Ni, Assembly of a rovibrational ground state molecule in an optical tweezer, *Phys. Rev. Lett.* **126**, 123402 (2021).
- [42] Y. Yu, K. Wang, J. D. Hood, L. R. B. Picard, J. T. Zhang, W. B. Cairncross, J. M. Hutson, R. Gonzalez-Ferez, T. Rosenband, and K.-K. Ni, Coherent optical creation of a single molecule, *Phys. Rev. X* **11**, 031061 (2021).
- [43] D. K. Ruttley, A. Guttridge, S. Spence, R. C. Bird, C. R. Le Sueur, J. M. Hutson, and S. L. Cornish, Formation of ultracold molecules by merging optical tweezers, *Phys. Rev. Lett.* **130**, 223401 (2023).
- [44] C. Zhang and M. R. Tarbutt, Quantum computation in a hybrid array of molecules and Rydberg atoms, *PRX Quantum* **3**, 030340 (2022).
- [45] K. Wang, C. P. Williams, L. R. B. Picard, N. Y. Yao, and K.-K. Ni, Enriching the quantum toolbox of ultracold molecules with Rydberg atoms, *PRX Quantum* **3**, 030339 (2022).
- [46] A. Guttridge, D. K. Ruttley, A. C. Baldock, R. González-Férez, H. R. Sadeghpour, C. S. Adams, and S. L. Cornish, Observation of Rydberg blockade due to the charge-dipole interaction between an atom and a polar molecule, *Phys. Rev. Lett.* **131**, 013401 (2023).
- [47] I. I. Beterov and M. Saffman, Rydberg blockade, Förster resonances, and quantum state measurements with different atomic species, *Phys. Rev. A* **92**, 042710 (2015).
- [48] N. Samboy, Long-range interactions between rubidium and potassium Rydberg atoms, *Phys. Rev. A* **95**, 032702 (2017).
- [49] J. S. Otto, N. Kjærgaard, and A. B. Deb, Strong zero-field Förster resonances in K-Rb Rydberg systems, *Phys. Rev. Res.* **2**, 033474 (2020).
- [50] J. M. Auger, S. Bergamini, and D. E. Browne, Blueprint for fault-tolerant quantum computation with Rydberg atoms, *Phys. Rev. A* **96**, 052320 (2017).
- [51] A. M. Farouk, I. I. Beterov, P. Xu, S. Bergamini, and I. I. Ryabtsev, Parallel implementation of CNOT^N and C²NOT² gates via homonuclear and heteronuclear Förster interactions of Rydberg atoms, *Photonics* **10**, 1280 (2023).
- [52] S. Weber, C. Tresp, H. Menke, A. Urvoy, O. Firstenberg, H. P. Büchler, and S. Hofferberth, Calculation of Rydberg interaction potentials, *J. Phys. B* **50**, 133001 (2017).
- [53] N. Šibalić, J. D. Pritchard, C. S. Adams, and K. J. Weatherill, ARC: An open-source library for calculating properties of alkali Rydberg atoms, *Comput. Phys. Commun.* **220**, 319 (2017).
- [54] D. Jaksch, J. I. Cirac, P. Zoller, S. L. Rolston, R. Côté, and M. D. Lukin, Fast quantum gates for neutral atoms, *Phys. Rev. Lett.* **85**, 2208 (2000).
- [55] A. Reinhard, T. C. Liebisch, B. Knuffman, and G. Raithel, Level shifts of rubidium Rydberg states due to binary interactions, *Phys. Rev. A* **75**, 032712 (2007).
- [56] A. Reinhard, K. C. Younge, T. C. Liebisch, B. Knuffman, P. R. Berman, and G. Raithel, Double-resonance spectroscopy of

- interacting rydberg-atom systems, *Phys. Rev. Lett.* **100**, 233201 (2008).
- [57] I. I. Ryabtsev, D. B. Tretyakov, I. I. Beterov, and V. M. Entin, Observation of the stark-tuned Förster resonance between two Rydberg atoms, *Phys. Rev. Lett.* **104**, 073003 (2010).
- [58] S. Ravets, H. Labuhn, D. Barredo, L. Béguin, T. Lahaye, and A. Browaeys, Coherent dipole-dipole coupling between two single Rydberg atoms at an electrically-tuned Förster resonance, *Nat. Phys.* **10**, 914 (2014).
- [59] K. Singer, J. Stanojevic, M. Weidemüller, and R. Coté, Long-range interactions between alkali Rydberg atom pairs correlated to the ns–ns, np–np and nd–nd asymptotes, *J. Phys. B* **38**, S295 (2005).
- [60] T. G. Walker and M. Saffman, Zeros of Rydberg–Rydberg Förster interactions, *J. Phys. B* **38**, S309 (2005).
- [61] S. Ravets, H. Labuhn, D. Barredo, T. Lahaye, and A. Browaeys, Measurement of the angular dependence of the dipole-dipole interaction between two individual Rydberg atoms at a Förster resonance, *Phys. Rev. A* **92**, 020701(R) (2015).
- [62] V. V. Shende and I. L. Markov, On the CNOT-Cost of TOFFOLI gates, *Quantum Inf. Comput.* **9**, 461 (2009).
- [63] Data available from <https://doi.org/10.15129/96cf2b15-7baa-4408-9687-66a5c4721f4b>.